Robust dehydrofluorination catalyst with host-guest structure between VOF$_x$ clusters and MgFe-LDF

Bing Liu , Yu Wang , Yunfan Huang , Lijia Liu , Yifan Wei , Yiwei Sun , Xiaoli Wei , Wenfeng Han [*]

State Key Laboratory Breeding Base of Green-Chemical Synthesis Technology, College of Chemical Engineering, Zhejiang University of Technology, Hangzhou 310014, China

ARTICLE INFO

ABSTRACT

A novel strategy for the preparation of metal fluoride catalyst with medium surface acidity is reported via anion exchange and host-guest structure. MgFe-CO$_3^{2-}$-LDH (layered double hydroxide) was selected as the host and NH$_4$VO$_3$ was selected as the guest. After interlamellar anion exchange and pre-fluorination treatment, the MgFe-VO$_3$-LDH is converted to MgFe-V-LDF (layered double fluorides). It exhibits high activity for the dehydrofluorination of 1,1,1,3,3-pentafluoropropane (HFC-245fa) to 1,3,3,3-tetrafluoropropene (HFO-1234ze), with HFC-245fa conversion of 93% which exceeded that of pure V$_2$O$_5$-F by roughly 9 times. After 50 h of reaction, no noticeable deactivation was detected. Overall, we present a potential strategy for creating effective metal-fluoride Lewis acid catalysts.

1. Introduction

Hydrofluorocarbons (HFCs) possess physicochemical properties similar to those of chlorofluorocarbons (CFCs) and are indispensable and functional chemicals in modern society [1,2]. It is usually used as refrigerants, blowing agents, aerosol propellants and polymer monomers, etc. For instance, 1,1,1,2-tetrafluoroethane (HFC-134a) has been widely used as refrigerant and blowing agents [3]. However, its global warming potential (GWP) is extremely high compared to that of CO$_2$. As a result, there is an urgent need to find other environmentally friendly alternatives to HFCs [4]. Fortunately, due to the presence of highly reactive C=C double bonds in their molecular structure, the hydrofluoroolefins (HFOs) have recently been considered as a new alternative to HFCs. Hence, the HFOs possess shorter atmospheric life time and a much lower GWP value [5]. Among all the HFOs products, 1,3,3,3-tetrafluoropropene (HFO-1234ze) is regarded to be the best alternative to HFC-134a due to its high cooling efficiency and good compatibility [6].

Currently, the best synthetic route for HFO-1234ze is the gas-phase dehydrofluorination of 1,1,1,3,3-pentafluoropropane (HFC-245fa). This process route exactly solves the problem of excess HFC-245fa capacity [7]. Since the C-F bond in the molecular structure of HFCs is extremely stable, the dehydrofluorination of HFCs is usually carried out under high temperature and extremely corrosive conditions and requires Lewis acid sites as the catalytic active centers [8]. Accordingly, the

metal fluorides such as AlF$_3$ [9], MgF$_2$ [10] and fluorinated Cr$_2$O$_3$ (F-Cr$_2$O$_3$) [11] have been used as catalytic materials which can exist stably in HF atmosphere. For dehydrofluorination reaction, the Lewis acid site is not only the active center, but it accounts for the carbon deposition [12]. For instance, Wuttke et al. [13] reported that the AlF$_3$ catalyst exhibited extremely high catalytic activity in the dehydrofluorination of 3-chloro-1,1,1,3-tetrafluorobutane reaction, but deactivates rapidly due to the strong Lewis acidity of the AlF$_3$. To improve the catalyst life, Pd and Ru were introduced into the AlF$_3$ and F-Cr$_2$O$_3$ catalysts as promoters, respectively [14]. However, this series of catalysts is very expensive and the catalyst lifetime is not long enough for the industrial application. Hence, combining the catalytic activity and stability, a relatively weak acid strength which is able to cleave the C-F band and avoid coke formation is a promising candidate as stable catalyst for dehydrofluorination reaction.

Magnesium fluoride (MgF$_2$) is an excellent host for doping other active metals (such as Cr, Al, and Fe) to enhance catalytic performance due to its high specific surface area and weak Lewis acid sites [15]. Among these metal additives, FeF$_3$ has often been used as a dopant to MgF$_2$, and its acid structure has been intensively investigated. For example, Kemnitz et al. [16] prepared a ternary nanoscopic FeF$_3$-MgF$_2$ catalyst with enhanced porosity catalyst via one-step fluorination method. Surface characterization confirmed the presence of medium-strong Lewis and Brønsted acid sites on the catalyst surface. The

---

FeF_3-MgF_2 catalysts were highly active in the isomerisation of citronellal to isopulegol due to the bi-acidity. In recent, Mao et al. [17] reported a Fe/nano-MgF_2 catalyst with excellent stability in HF atmosphere and possessed larger amounts of medium acid sites. And the Fe/nano-MgF_2 demonstrated much higher catalytic activity than the traditional fluorinated Cr_2O_3 on the fluorination of 1,1,1,3-tetrachloropropane reaction. It is well known that vanadium oxide is a versatile additive, and the introduction of vanadium species can effectively increase the surface acidity of the catalyst [18]. For example, Kemnitz et al. [19] found that the pure MgF_2 contains only a few Lewis acid sites, whereas MgF_2/VF_3 possesses many Lewis acid sites. Similarly, Luo et al. [20] found that the activity of V/MgF_2 catalyst in the HFC-245fa dehydrofluorination reaction was much higher than that of pure MgF_2.

According to the above literature, we believe that the combination of MgF_2, FeF_3 and vanadium oxide will have high catalytic activity in the gas-phase dehydrofluorination reaction. In our previous work [21], we selected MIL-101-Cr as the host and $(NH_4)_3AlF_6$ as the guest. With calcination temperature of 350 °C, the AlF_3 nanocluster catalyst (named as AlF_3 @MIL-101–350) with quasi-MOFs structure confinement was achieved, which exhibited excellent stability towards gas dehydrofluorination. Inspired by this, we still adopt the host-guest strategy and choose layered double hydroxides (LDHs) materials as the host. LDHs are a type of anionic clay of inorganic layered materials which can be represented by the general formula $[M^{2+}_{1-x}M^{3+}_x(OH)_2]^{x+}[A_{x/n}]^{n-}\cdot mH_2O$. In the general formula, M^{2+} (such as Mg^{2+}, Zn^{2+} Co^{2+} or Ni^{2+}) and M^{3+} (such as Fe^{3+}, Cr^{3+}, Al^{3+} or Ga^{3+}) are divalent and trivalent metal cations, respectively, which form the positively charged laminate [22]. Remarkably, negatively charged interlayer anions repel each other and are electrostatically adsorbed near the M^{3+} site in positively charged LDH plates. Hence, for LDHs materials, due to their unique characteristics, such as the extensive tunability of the types of metal cations, the surface tunable basicity, and the nature of interlayer ion-exchange ability, the LDHs have gained a lot of attention in the field of catalysis as a host-guest combinations. For instance, Liu et al. [22] used the NiFeAl-LDH as a precursor to obtain NiFe-LDH with cation vacancies after etching, and then used it as a support to prepare a series of Ru/NiFe-LDH catalysts. Furthermore, the isolated Ru atoms anchored by cation vacancies facilitate the desorption of benzaldehyde, thus leading to the Ru/NiFe-LDH catalyst possessing a very high TOF value (1331 h^{-1}) in the benzyl alcohol oxidation reaction. Huang et al. [23] similarly reported that doping Cerium in MgAl-LDH could effectively enhance the redox performance of the catalyst. Hang et al. found that doping Cerium in MgAl-LDH materials could effectively enhanced the redox ability and modified acid-base sites of the catalyst. In particular, the $Mg_3Al_{0.9}Ce_{0.1}$ catalyst exhibited excellent catalytic performance in the ketonization reaction of acetic acid.

Thus, in the present work, we selected MgFe-CO_3^{2-}-LDH as the host and the VO_3 as the guest, and the MgFe-VO_3-LDH was successfully obtained via anion exchange and space-confined strategy. The structure of MgFe-VO_3-LDH was carefully investigated by XRD, FT-IR and Raman characterization techniques. After pre-fluorination heat treatment, the MgFe-VO_3-LDH transformed to MgFe-V-LDF (layered double fluorides), and the interlayer VO_3 anion was converted to highly dispersed VOF_x species, as evidenced by FT-IR, Raman and XRD characterization results. Following the addition of VOF_x species, the large amounts of weak and medium Lewis acid sites were derived. Consequently, the MgFe-V-LDF catalyst exhibits high and stable catalytic performance in the gas-phase dehydrofluorination of HFC-245fa. In-depth research was done on the structure-activity relationship between the host (laminate of MgFe-LDF) and guest (interlayer VOF_x). SEM, EDX-Mapping and BET were adopted for analysis of the distribution of VOF_x in the MgFe-LDF. Additionally, XPS and EPR were used to define the interaction between MgFe-LDF and VOF_x nanoclusters. Since the Lewis acid sites were the active centers for the dehydrofluoriantion, the acidic properties of various catalysts were measured with the NH_3-TPD and pyridine-FTIR.

2. Experimental

2.1. Synthesis of MgFe-LDF

The MgFe-CO_3^{2-}-LDH precursors was synthesized by a conventional coprecipitation method [24]. In a typical procedure, solution A contains 100 mL of ultrapure water, magnesium nitrate (0.075 mol), and iron nitrate (0.025 mol); solution B contains 60 mL of ultrapure water, NaOH (0.2 mol), and Na_2CO_3 (0.05 mol). At room temperature, solutions A and B were added dropwise to a three-necked flask. The process lasts 40 min, and the pH of the reaction system was kept around 9.5. After that, the slurry was aged at 65 °C for 24 h and then washed by centrifugation with ultrapure water. Then, the product was dried at 80 °C for 24 h, the MgFe-CO_3^{2-}-LDH was obtained and denoted as MgFe-LDH. To obtain the layer bimetallic fluoride catalysts, 3 g MgFe-LDH and 10 g NH_4F were mixed mechanically and calcined at 400 °C for 4 h in air at a heating rate of 3 °C min^{-1}. The final sample was expressed as MgFe-LDF. The preparation process of MgFe-LDF was shown in Scheme S1.

2.2. Synthesis of MgFe-M-LDF

The MgFe-VO_3^--LDH was obtained via anion exchange method using MgFe-CO_3^{2-}-LDH as the precursor. 4 g MgFe-CO_3^{2-}-LDH and 1.8 g NH_4VO_3 were poured into 400 mL the deionized water, and using nitric acid to maintain the solution's pH at about 4. After stirring at 65 °C for 24 h under the protection of N_2, intercalation CO_3^{2-} of MgFe-CO_3^{2-}-LDH was replaced by VO_3^-. After centrifuging the crude product three times with ultrapure water, the MgFe-VO_3^--LDH was eventually obtained. Then the product was dried at 80 °C for 24 h and denoted as MgFe-V-LDH. Finally, 3 g MgFe-V-LDH and 10 g NH_4F was mixed mechanically and calcined at 400 °C for 4 h in air. The final sample was expressed as MgFe-V-LDF. The preparation process of MgFe-V-LDF was shown in Scheme 1. To investigate the influence of different guest anion on the performance of MgFe-M-LDF catalysts, MgFe-Al-LDF and MgFe-Ti-LDF were prepared with similar procedure as MgFe-V-LDF, with 1.8 g NH_4VO_3 was replaced by 3 g $(NH_4)_3AlF_6$ or $(NH_4)_3TiF_6$.

2.3. Synthesis of V/MgFe-LDF and V_2O_5-F

To investigate the difference between VO_3^- ion intercalation and supporting, the VO_3^-/MgFe-LDH was prepared by an impregnation method. Typically, 100 mL of ultrapure water was combined with 2 g of dehydrated MgFe-LDH and 0.5 g of NH_4VO_3 and vigorously stirred for 12 h. Subsequently, the solid product was washed three times by centrifugation with ultrapure water to remove excess NH_4VO_3 and dried at 80 °C for 12 h. Then, the VO_3^-/MgFe-LDH was obtained and denoted as V/MgFe-LDH. Finally, V/MgFe-LDH and 10 g NH_4F was mixed mechanically and calcined at 400 °C for 4 h to afford V/MgFe-LDF. The preparation process of V/MgFe-LDF was shown in Scheme S2. For comparison, the pure V_2O_5-F catalyst was prepared by pre-fluorination heat treatment of V_2O_5. Typically, 5 g V_2O_5 and 10 g NH_4F was mixed mechanically and calcined in air at 400 °C for 3 h.

2.4. Characterization of catalysts

Surface areas of various LDHs and LDFs were measured using the Micromeritics ASAP 2020 N_2 adsorption-desorption isotherm at − 196 °C. Powder X-ray diffraction (XRD) was used to characterize the crystal structure of various samples with a Thermo ARL X'TRA diffractometer (Cu-K radiation). Scanning electron microscope (SEM) and transmission electron microscopy (TEM) techniques were used to investigate the micromorphology and distribution of V species in various samples, and both characterization methods were carried out on the FESEM HitachiS-470 and the FEI Tecnai G2 F30, respectively.

The surface chemical group of various samples was measured by FT-IR spectroscopy on a Nexus 670, and the wave number ranged between
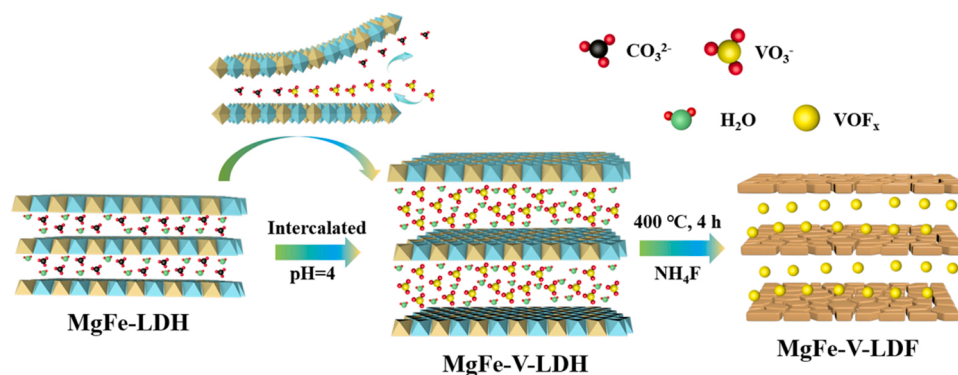
Scheme 1. Schematic illustration of the preparation of MgFe-V-LDF.

4000 and 400 cm^{-1}. Raman spectra were collected on a Horiba Scientific spectrometer with a 532 nm laser. At room temperature, the oxygen vacancy of various LDFs and V_2O_5-F was measured using an electron paramagnetic resonance (EPR) spectrometer from Bruker. X-ray photoelectron spectroscopy (XPS) techniques were used to determine the chemical state of various LDFs and V_2O_5-F. The measurements were made using an ESCALAB210 spectrometer, monochromatized Mg Kα as the excitation source, and C 1 s (284.6 eV) as the reference line.

Temperature-programmed desorption of ammonia (NH_3-TPD) techniques were used to determine the surface acidity of various LDFs catalysts. The experiment was performed on a self-built instrument. 0.1 g sample was typically weighed into a U-shaped quartz tube. Prior to the test, the sample was heated to 300 °C in a helium atmosphere (at a rate of 10 °C min^{-1}) for 1 h to remove water and other impurities, then cooled to room temperature. Following that, to complete the NH_3 adsorption, an NH_3/He mixture gas (10% in helium) was introduced into the tube for 30 min. The system was then heated to 100 °C and switched to a helium atmosphere purge for 1 h to remove the weakly adsorbed NH_3. Finally, while the sample was being heated from 100° to 800°C at a rate of 10 °C min^{-1}, a thermal conductivity detector was used to monitor it online. The surface acidity of various LDF catalysts was further determined by Py-IR on a Nexus 670 FTIR spectrometer. Prior to the experiment, the sample was heated to 350 °C for 2 h to remove the water, then cooled to 150 °C. The background spectrum was also collected. After cooling to room temperature, the sample was adsorbed with pyridine for 30 min. Finally, the samples were heated to 150 °C in a helium atmosphere and purged for 30 min before recording spectra in the 1200–1700 cm^{-1} range.

2.5. Catalytic activity evaluation

The catalytic experiment was carried out at atmospheric pressure in a conventional fixed-bed flow reactor (12 mm (i.d.) × 400 mm). Typically, 1 mL of catalysts were placed in the reactor which equipped with a thermal couple to detect the actual reaction temperature. Firstly, the catalyst bed was heated up to 350 °C and maintained for 2 h in N_2 flow (20 mL min^{-1}) to remove water and impurities from the catalyst surface. Then the N_2 flow was stopped and a mixture of N_2 and HFC-245fa (HFC-245fa/N_2 of 4/10, total flow rate of 12.5 mL min^{-1}, GHSV of 750 h^{-1}) was introduced to the reactor, where N_2 was used as an internal standard for volume correction. The reaction effluent was washed with aqueous KOH solution to remove the HF. Finally, the obtained products were analyzed online using gas chromatography (Jiedao GC1690) with a PoraPLOT Q column (3 mm * 5 m) and a thermal conductivity detector (TCD).

3. Results and discussions

3.1. Catalytic performance of MgFe-LDF and MgFe-M-LDF catalysts

To investigate the effect of interlayered metal on the catalytic dehydrofluorination of HFC-245fa, Fig. 1a and Fig. S1 show the catalytic behaviors of the MgFe-LDF and MgFe-M-LDF catalysts at reaction temperature of 350 °C. HFC-245fa conversion on the MgFe-LDF declines from 47% to 4% after 20 h. Similarly, MgFe-Al-LDF and MgFe-Ti-LDF gradually deactivate as the reaction proceeds, with HFC-245fa conversion declining from 49% and 40–27% and 30% in 20 h, respectively. Although both of MgFe-Al-LDF and MgFe-Ti-LDF deactivate rapidly, their deactivation rates were slower than those of MgFe-LDF. Clearly, AlF_6^{3-} and TiF_6^{3-} intercalation into the interlayer of MgFe-LDH only slightly improves the catalytic performance. By contrast, the catalytic activity was significantly enhanced after the introduction of the intercalated VO_3^- ion. The MgFe-V-LDF catalyst exhibits the highest conversion as high as 93%. After 50 h on stream, no noticeable deactivation was detected, indicating its good stability. As shown in Fig. 1b, all of the catalysts exhibit very high selectivity for HFO-1234ze, with trans-HFO-1234ze selectivity of 80% and cis-HFO-1234ze selectivity of 20%, respectively. The screening of various intercalation anion reveals that the VO_3^- could be a promising candidate for this reaction and thereafter detailed experiments are focused on MgFe-V-LDF.

3.2. Characterization of LDH precursors

To further investigate the mechanism of such high dehydrofluorination activity over MgFe-V-LDF, the structure of its precursor MgFe-VO$_3$-LDH was characterized by XRD. Fig. 2a shows that both of MgFe-LDH and MgFe-V-LDH all possess the characteristic diffraction peaks of LDHs materials [25]. The (003), (006), (009), and (015) planes of the MgFe-LDH are assigned to the diffraction peaks at 11.3, 22.8, 33.9 and 38.1 °. Additionally, the sharp and symmetric diffraction peaks indicate that MgFe-LDH have a high crystallinity. In particular, a clear double peak was detected around 59 °, indicating a well symmetry of the MgFe-LDH crystalline. The intensity of all diffraction decreases dramatically for MgFe-V-LDH, indicating that LDH has a low crystallinity after the intercalation process. Meanwhile, the diffraction peak of (003) plane in MgFe-V-LDH shifts to a lower angle and becomes wider, indicating the successful insertion of VO_3^- into the MgFe-LDH interlayer [26].

MgFe-LDH and (b) MgFe-V-LDH

The structure schematic of MgFe-LDH and MgFe-V-LDH were shown in Fig. 3, and the specific structural arguments were listed in Tab. S1. As shown in Fig. 3a, The basal spacing (D-spacing; d_{003}) of MgFe-LDH is 0.78 nm, which is similar with that of LDHs materials in CO_3^{2-} form [27]. However, after intercalation with the VO_3^- anions, the basal spacing of MgFe-V-LDH is increased slightly to 0.85 nm (Fig. 3b), and it confirms
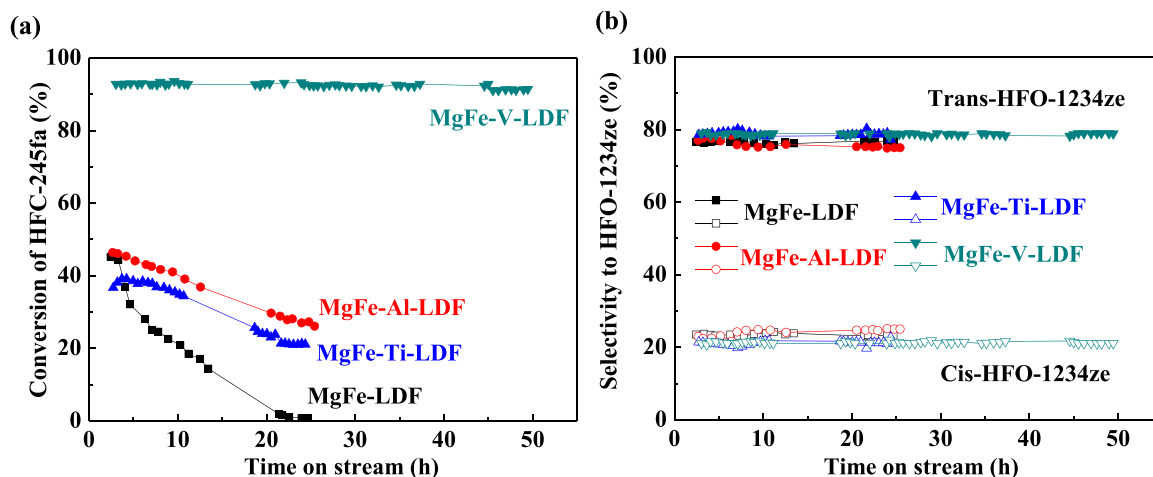
Fig. 1. (a) Conversion of HFC-245fa and (b) Selectivity to trans-HFO-1234ze and cis-HFO-1234ze over MgFe-LDF and MgFe-M-LDF catalysts (reaction condition: atmospheric pressure, GHSV = 750 h^{-1}, N$_2$/HFC-245fa = 10/4).
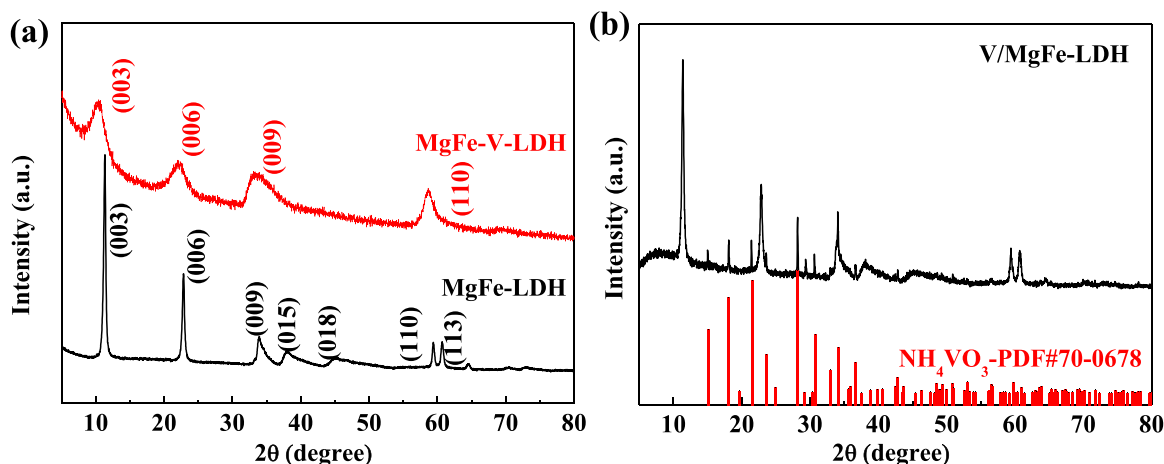

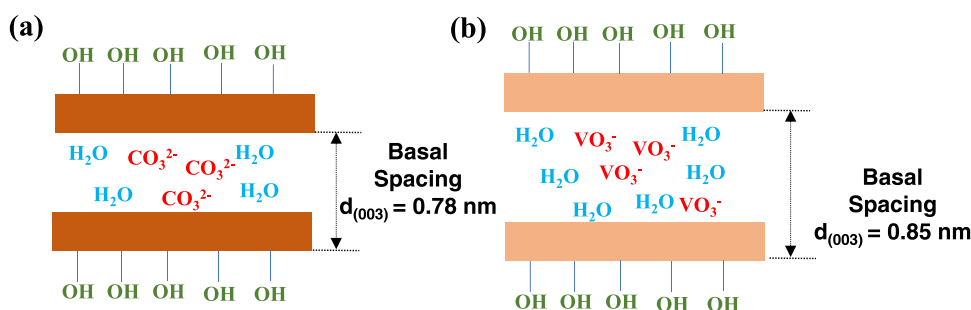**Fig. 2.** XRD patterns of (a) MgFe-LDH and MgFe-V-LDH and (b) V/MgFe-LDH.

Fig. 3. Chemical structure of a typical LDH with different interlayer anions of (a).

that the VO$_3^-$ anions intercalated successfully into the interlayer of MgFe-LDH. It is worth noting that the position of diffraction peak of (110) is not significantly shifted, suggesting that the intercalation of VO$_3^-$ does not lead to a change in the laminate composition of MgFe-LDH [28]. Fig. 2b demonstrates the XRD patterns of the V/MgFe-LDH. The position and intensity of the characteristic diffraction peaks of the support (MgFe-LDH) remain unchanged, and while the XRD diffraction peaks of NH$_4$VO$_3$ are clearly detected. It indicates that the NH$_4$VO$_3$ was unevenly distributed on the surface of MgFe-LDH with large particles.

To investigate the variation in the specific surface and pore structure of MgFe-LDH after the introduction of VO$_3^-$ by intercalation and loading,

the N$_2$ physisorption experiments were performed on MgFe-LDH, MgFe-V-LDH and V/MgFe-LDH. As displayed in Fig. S2a, the pristine MgFe-LDH exhibits type V isotherm and H4 hysteresis, which are typical of mesoporous materials, and it is further confirmed by its pore size distribution (Fig. S2b). As listed in Table 1, the surface area and pore volume of pristine MgFe-LDH are 72 m^2 g^{-1} and 0.68 cm^3 g^{-1}, respectively. However, after VO$_3^-$ anion was intercalated into the interlayer of MgFe-LDH, the textural properties are altered significantly. Type IV isotherms and H2 hysteresis loops are present in MgFe-V-LDH, demonstrating the coexistence of both mesoporous and microporous materials. The surface area of MgFe-V-LDF increases to 165 m^2 g^{-1}, which is

Table 1

Surface area and porosity of MgFe-V-LDH, MgFe-LDH and V/MgFe-LDH.

Samples	Surface area ($m^2 \cdot g^{-1}$)	Pore volume ($cm^3 \cdot g^{-1}$)	Average pore diameter (nm)
MgFe-V-LDH	165	0.92	7.3
MgFe-LDH	72	0.68	37.9
V/MgFe-LDH	50	0.46	37.1

almost doubled compared with pristine MgFe-LDH, and pore volume also increases to 0.92 cm^3 g^{-1}. It could be attributed to the interlayer anion. For MgFe-LDH CO_3^- possesses stronger electronegative and has a greater electrostatic gravitational force to the laminate. Therefore, the layer spacing of MgFe-LDH is narrower resulting in relatively low surface area and pore volume. Nevertheless, the weak electronegativity of VO_3^- leads to a wider layer spacing of MgFe-V-LDH, leading to higher specific surface area. This is also consistent with the XRD results that the VO_3^- anions inserted successfully into the interlayer of MgFe-LDH. After the addition of VO_3^- by loading, the surface area and pore volume decreased dramatically to 50 m^2 g^{-1} and 0.46 cm^3 g^{-1}, respectively. It indicates that NH_4VO_3 in V/MgFe-LDH is mainly distributed on the surface of MgFe-LDH rather than between the laminates.

The morphology of various precursor LDHs samples were investigated with SEM technique and the results are displayed in Fig. S3. The pristine MgFe-LDH was composed of small particles in close proximity. By contrast, after VO_3^- anions intercalated into the interlayer of MgFe-LDH, MgFe-V-LDH accumulates from fine lamellar particles to flower-like clusters, and the gap between the lamellar particles is wider (Fig. S3c-d). Expectedly, no NH_4VO_3 particles can be observed. It shows that the VO_3^- anion was successfully inserted into the interlayer of MgFe-LDH, which is also consistent with the BET results. However, as shown in Fig. S3e-f, no significant changes were observed in the microscopic morphology of V/MgFe-LDH compared to pristine MgFe-LDH. The EDS analysis implies that the molar ratio of Mg/Fe in MgFe-LDH is 3.12, which is close to the feeding value during preparation, indicating the high purity of the prepared hydrotalcite (Tab. S2). Similarly, after intercalation with the VO_3^- anions, the Mg/Fe molar ratio in MgFe-V-LDH is also 3.08, similar with MgFe-LDH. It indicates that the intercalation of VO_3^- does not lead to a change in the composition of the main laminate of MgFe-LDH. It is worth noting that C content of MgFe-V-LDH is much lower than that of MgFe-LDH and V/MgFe-LDH, only about 13.5%. This discrepancy could be attributed to that the large amount of interlayer CO_3^- being replaced by VO_3^- intercalation. It is reinforced by that the V content of MgFe-V-LDH was 5.4%, which was similar to that of V elements V/MgFe-LDH (5.8%). However, the XRD and SEM results showed that NH_4VO_3 phase was not detected in MgFe-V-LDH, indicating that the V species was highly dispersed in MgFe-V-LDH.

The surface chemical groups of MgFe-LDH, MgFe-V-LDH, and V/MgFe-LDH were analyzed with FT-IR experiments. According to Fig. 4a, the peak at 3495 cm^{-1} was assigned to the stretching vibrations of the -OH groups in the structure of pristine MgFe-LDH laminates and interlayer water molecules [29]. All three samples detected significant vibrations peaks near 1355 and 1645 cm^{-1}. These two peaks are attributed to the interlayer CO_3^{2-} anion and the LDHs interlayer water molecule's H-OH bending vibration, respectively [30]. Especially, the intensity of the bending vibration peak of O-OH of interlaminar water molecules in MgFe-V-LDH was significantly stronger than that of MgFe-LDH, and while the intensity of the stretching vibration peak of interlayer CO_3^- was much weaker than that of MgFe-LDH. Due to the weaker electronegativity of VO_3^- than CO_3^-, MgFe-V-LDH possesses a broader layer spacing and a larger number of interlaminar water molecules. While, due to the intercalation substitution of VO_3^- for CO_3^-, the intensity of the stretching vibration peak of interlayer CO_3^{2-} decreases significantly. As for MgFe-V-LDH, the V═O stretching vibration peak of VO_3^- was also detected at 920 cm^{-1} [31]. Clearly, the presence of the V═O stretching band and the weakening of the intensity of the CO_3^- absorption band in the FT-IR spectrum of MgFe-V-LDH coincide with the successful intercalation of the VO_3^- anion. Lower wavenumber band spectra of 705 and 580 cm^{-1} correspond to Mg-O and Fe-O vibration bands, respectively [32]. Notably, the NH_4 vibrational band attributed to bulk NH_4VO_3 was detected at 3200 cm^{-1} in V/MgFe-LDH, which is also observed in pure NH_4VO_3 (Fig. S4) [33]. It further confirms that NH_4VO_3 distributed on the surface MgFe-LDH with larger particles for V/MgFe-LDH. This argument is reinforced by Raman data. As illustrated in Fig. 4b , for the pristine MgFe-LDH, the distinct bands at 140, 285, and 532 cm^{-1} can be ascribed to M-OH stretching modes in MgFe-LDH laminates. The characteristic peak located at 1055 cm^{-1} is assigned to the interlaminar CO_3^- [34]. In V/MgFe-LDH, not only all characteristic peaks of MgFe-LDH are detected, but also V-O-V stretching vibrations are detected at 200–350 and 650 cm^{-1}, as well as V═O stretching vibrations at 900, 930 and 1040 cm^{-1} [35]. These Raman bands are also observed in pure NH_4VO_3 (Fig. S5), which further confirms that the NH_4VO_3 is present in the V/MgFe-LDH with large particles. However, for MgFe-V-LDH, the distinct bands belonging to V-O and V═O are weak, indicating that the V species are highly dispersed in MgFe-V-LDH. In addition, the characteristic peak of CO_3^- is not detected at 1050 cm^{-1} for MgFe-V-LDH, which further suggesting that the VO_3^- anions are successfully confined between the LDHs lamellae.
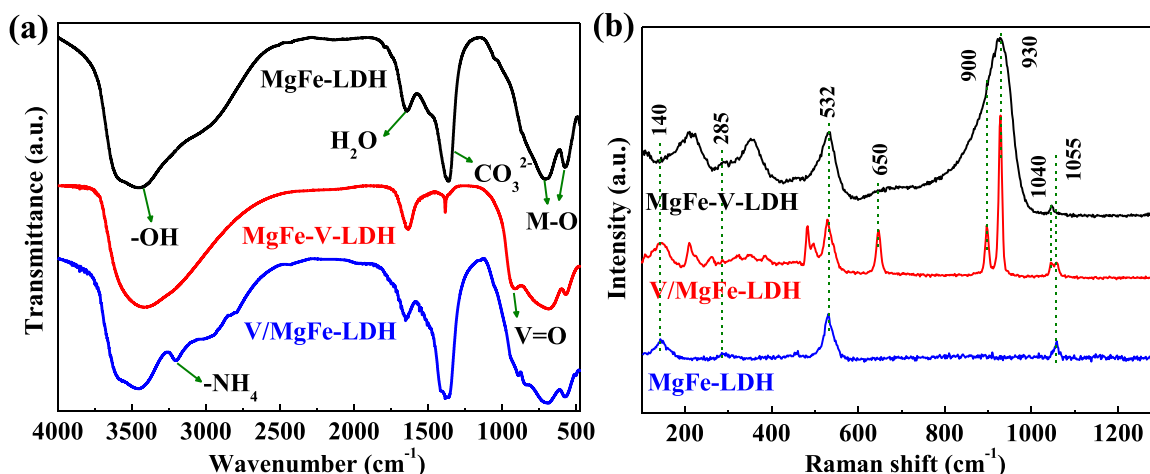

Fig. 4. (a) FT-IR spectra and (b) Raman spectra of MgFe-V-LDH, MgFe-LDH and V/MgFe-LDH.

3.3. Characterization of LDF catalysts

To investigate the phase composition of different LDHs precursors after pre-fluorination treatment, the XRD experiments are employed for pure MgFe-LDF, MgFe-V-LDF and V/MgFe-LDF catalysts. As displayed in Fig. 5a, distinctive diffraction peaks of crystalline MgF_2 (JCPDS No. 70–2269) were detected at 27.2, 38.9, 40.4, 43.7, and 53.5° etc. in pure MgFe-LDF. Concurrently, the characteristic peaks of Fe_2O_3 (JCPDS No. 85–0599) were also detected at 24.1, 33.2 and 49.4 °. Clearly, $Mg(OH)_2$ in MgFe-LDH laminate was converted to MgF_2 by fluorination. $Fe(OH)_3$ is pyrolyzed to Fe_2O_3. After the introduction of VO_3^- by supporting for V/MgFe-LDF, these diffractions of MgF_2 and Fe_2O_3 remain with lower intensities, indicating that the presence of V species inhibits the formation of MgF_2 and Fe_2O_3 crystallites (Fig. 5b). In addition, the diffraction peaks of V_2O_5 produced by the pyrolysis of NH_4VO_3 are detected at 20.3 and 26.2 ° in V/MgFe-LDF (JCPDS No. 77–2418), indicating that V_2O_5 is distributed on MgFe-LDF with large particles. However, only the characteristic peaks of MgF_2 and Fe_2O_3 were detected in the MgFe-V-LDF, and no characteristic peaks of V_2O_5 or other V species are detected, indicating that the particle sizes of V species were too small to be detected by XRD (Fig. 5b). Clearly, during fluorination, VO_3^- was pyrolyzed to V_2O_5 or other V species and confined between the lamellae for MgFe-V-LDF. Due to the confinement, V_2O_5 or other V species were highly dispersed in MgFe-V-LDF. It has been reported in the literature that the structural state of vanadium oxides is closely related to their particle size [36]. The small vanadium oxide particles are dominated by isolated VO_4 tetrahedral species, whereas large grains of vanadium oxide are exhibited with chains of $(VO_3)_n$ or crystalline V_2O_5. Strong diffraction peaks are detected in pure V_2O_5-F that are in good agreement with those of crystalline V_2O_5 (Fig. S6).

As shown in Tab. S3, after pre-fluorination treatment, the surface area of various LDF catalysts were much lower than those of the corresponding LDH precursors. In addition, the surface area and pore volume of MgFe-V-LDF (74 m^2 g^{-1} and 0.38 cm^3 g^{-1}) outclasses than those of pure MgFe-LDF 54 m^2 g^{-1} and 0.22 cm^3 g^{-1}) and V/MgFe-LDF (40 m^2 g^{-1} and 0.19 cm^3 g^{-1}), respectively. All the three samples show type V isotherms and H3 hysteresis (Fig. S7a), indicating that all LDF catalysts are mesoporous materials with stacked plate-like particles, and it is further confirmed by its pore size distribution (Fig. S7b).

To investigate the transformation in the microscopic morphology of various LDHs precursors after pre-fluorination treatment, the SEM technique was measured for pure MgFe-LDF, MgFe-V-LDF and V/MgFe-LDF. As illustrated in Fig. S8a-b, after pre-fluorination treatment, pristine MgFe-LDH transforms from the initial particle cluster to a platelet shaped MgFe-LDF. Similarly, the morphology of MgFe-V-LDF is analogous to that of MgFe-LDF (Fig. S8c-d) with thinner layers, which is also

consistent with the BET result that MgFe-V-LDF has a higher specific surface area. In addition, no obvious V_2O_5 particles were observed in MgFe-V-LDF, indicating that the V species were highly dispersed in MgFe-V-LDF. Fig. S8e-f showed the SEM images of V/MgFe-LDF, where not only the platelike structure of MgFe-LDF but also the agglomerated V_2O_5 particles can be observed.

The TEM method was used to further explore the distribution of V species in the MgFe-LDF. As shown in Fig. S9a1-a2, pure MgFe-LDF exhibited a plate-like morphology formed by the accumulation of fine particles. The (111) plane of MgF_2 was observed in Fig. S9a3, which is consistent with the XRD results. Similarly, MgFe-V-LDF is also a plate-like structure consisting with small particles. Compared with MgFe-LDF, MgFe-V-LDF has a more pronounced lamellar structure with wider layer spacing (Fig. S9b1-b2), which consistent with the BET results (Tab.S3). It further confirms that the V species is confined between the laminates of MgFe-LDF. Simultaneously, the (110) plane of MgF_2 is also observed in MgFe-V-LDF, but no crystal planes of V_2O_5 particles are detected (Fig. S9b3). For V/MgFe-LDF, there is not only plate morphology but also some irregularly shaped V_2O_5 particles accumulated on the surface of the plate (Fig. S9c1-c2). In the lattice stripe analysis, the (110) plane of MgF_2 and the (001) plane of V_2O_5 are both observed in Fig. S9c3, which is consistent with the XRD results.

FTIR technique was used to characterize the surface chemical groups of various LDF catalysts, and the results are shown in Fig. 6a. Due to the pre-fluorination treatment, the water molecules and anions of LDHs interlayer decompose and were converted to the corresponding metal fluorides and oxides. The vibrations peak of interlayer water molecules at 1630 cm^{-1} almost disappear for all three LDF catalysts, and while the peak belonging to metal fluorides such as Mg-F at 447 cm^{-1} are detected [37]. Two new bands for the V/MgFe-LDF are attributed to the bulk V_2O_5 specific V-O-V bridge and V=O stretching vibrations at 820 and 900 cm^{-1}, respectively [31]. These two vibration bands are also detected in the V_2O_5-F and are more pronounced (Fig. S10). By contrast, for MgFe-V-LDF, the signal peaks of V=O and O-V-O stretching vibrations were very weak, implying that the V_2O_5 or other V species were highly dispersed in MgFe-V-LDF. This phenomenon is also consistent with the XRD results that the highly dispersed vanadium oxides are composed of with VO_4 tetrahedra, and the large particle size vanadium oxides are exhibited with V_2O_5 crystals. This conclusion is further supported by Raman results (Fig. 6b). For pure MgFe-LDF, following pre-fluorination treatment, the M-OH (Fe-OH and Mg-OH) bands between 400 and 800 cm^{-1} in MgFe-LDF almost disappear. For the V/MgFe-LDF, the broad bands at 278 and 380 cm^{-1} and the obvious bands in the 800–1000 cm^{-1} region, are attributed to V-O-V and V=O stretching modes of crystalline V_2O_5, respectively [38]. It is further confirmed with the results of the Raman spectra of pure V_2O_5-F (Fig. S11). On the
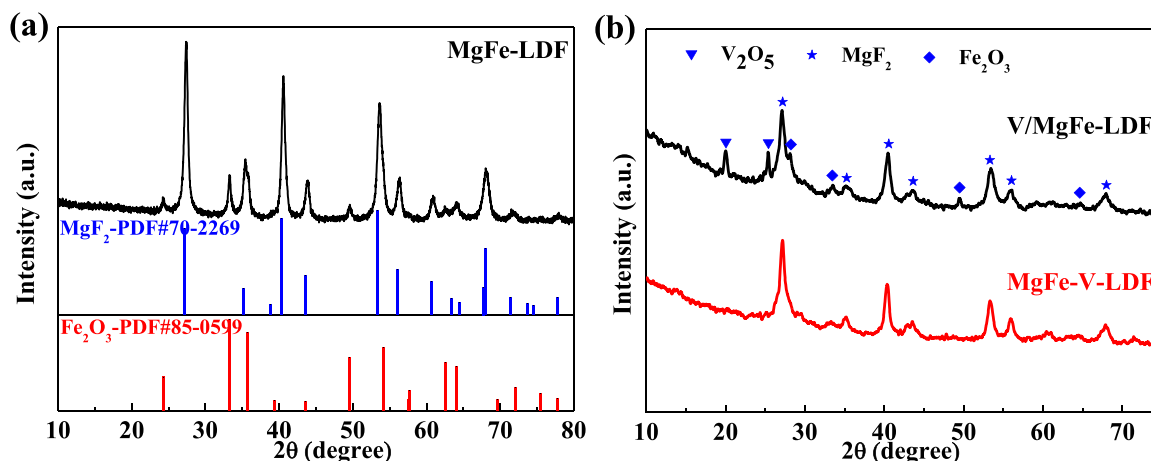

Fig. 5. XRD patterns of (a) MgFe-LDF and (b) MgFe-V-LDF and V/MgFe-LDF.
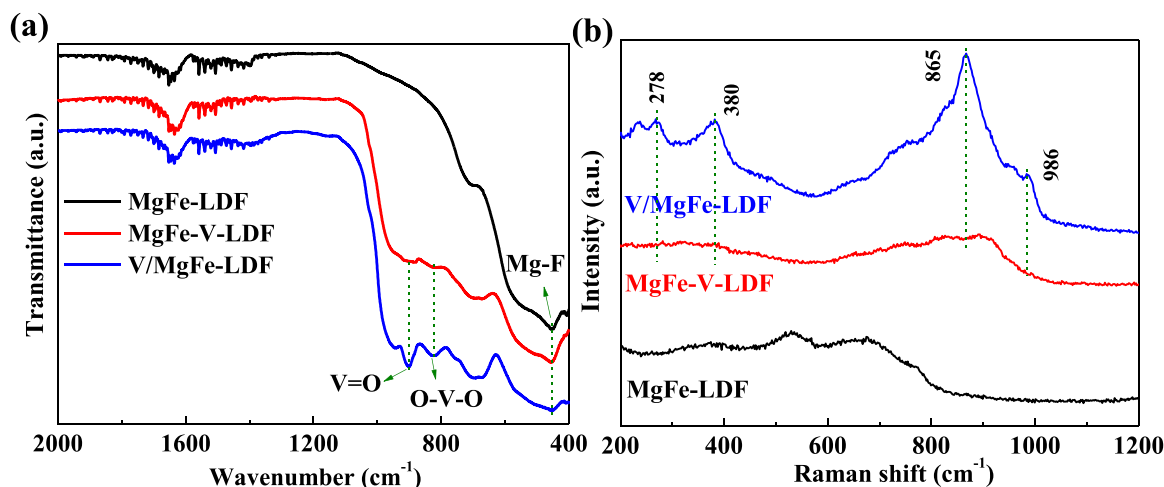
Fig. 6. (a) FT-IR spectra of and (b) Raman spectra of MgFe-V-LDF, MgFe-LDF and V/MgFe-LDF.

contrary, the typical vibration bands about V_2O_5 in MgFe-V-LDF is very weak, and the vibration peaks at 278 and 380 cm^{-1} disappear. Simultaneously, the bands in the 800–1000 cm^{-1} range broaden significantly. Combining the results of Raman spectroscopy and XRD (Fig. 6b), we suggest that the V_2O_5 species, which are highly dispersed in the MgFe-V-LDF, are transformed into species with weaker Raman spectral signals after pre-fluorination treatment.

From the above XRD results (Fig. 5b), some of the characteristic peaks of Fe_2O_3 in MgFe-V-LDF disappear. This may be caused by the transformation of Fe_2O_3 to some new Fe species. To verify the above discussion, the chemical states of Fe was investigated by XPS techniques. Fig. 7a demonstrates the Fe $2p_{3/2}$ XPS spectra for these LDF catalysts. The two peaks at about 711 and 716 eV are ascribed to the Fe-O of Fe_2O_3 and the Fe-F of FeF_3, respectively [39,40]. Clearly, Fe_2O_3 in the

MgFe-LDF was partly transformed to FeF_3 during pre-fluorination treatment. It has been reported in the literature that cubic metal oxides, such as α-Al_2O_3 and α-Fe_2O_3, are also partially fluorinated to the corresponding metal fluorides in a high-temperature HF atmosphere, which is also thermodynamically favorable [41]. The relative contents of Fe species on various LDF catalyst surface were calculated with XPS data, and the results are listed in Tab. S4. Interestingly, after the introduction of V species, the concentration of surface FeF_3 species in V/MgFe-LDF and MgFe-V-LDF increase from 19.8% (MgFe-LDF) to 24.1% and 35.3%, respectively. Clearly, the presence of V-Fe interaction facilitates the fluorination of Fe_2O_3. In particular, MgFe-V-LDF possesses the highest FeF_3 concentration, with a molar ratio of FeF_3/Fe_2O_3 as high as 0.53. Clearly, significant shift in binding energy of Fe-O and Fe-F peaks for MgFe-V-LDF to higher binding energy indicates a stronger
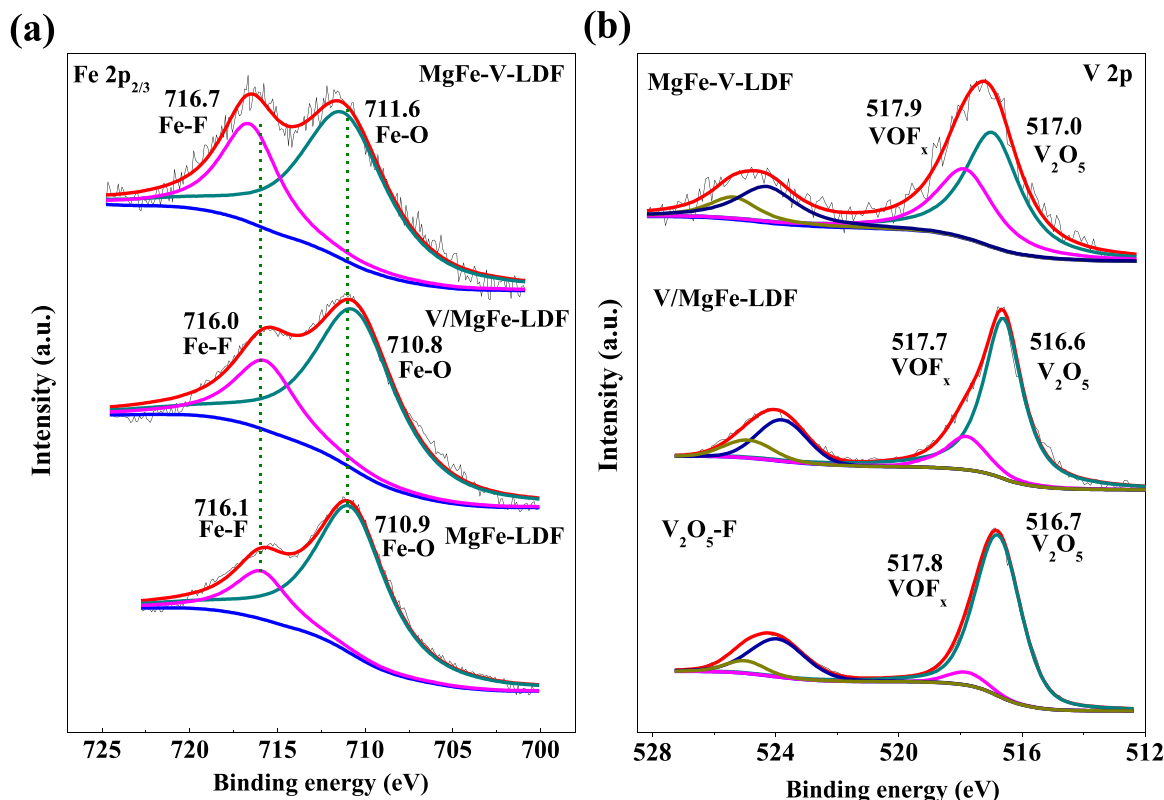

Fig. 7. (a) Fe $2p_{3/2}$ XPS spectra of MgFe-V-LDF, MgFe-LDF and V/MgFe-LDF and (b) V 2p XPS spectra of MgFe-V-LDF, V/MgFe-LDF and V_2O_5-F.

interaction between V and Fe in MgFe-V-LDF. From the Raman results (Fig. 6b), a distinct V_2O_5 signal peak is detected in V/MgFe-LDF. However, the signal peak of V_2O_5 species in MgFe-V-LDF is very weak. Therefore, the chemical environment of V species in representative samples was further investigated using the XPS technique, and the results are demonstrated in Fig. 7b. Two components with binding energies of 517.0 and 517.9 eV were observed in the MgFe-V-LDF catalysts, which belong to V_2O_5 species [42] and another V species with much lower electron density, respectively. The presence of this low electron density V species has been linked to the formation of VOF_x species, in which electrons in V atoms are transferred to F atoms due to F atoms' higher electronegativity [20]. The formation of VOFx species is attributed to that V_2O_5 which highly dispersed in MgFe-V-LDF which can be partially fluorinated during pre-fluorination treatment. The spectra of V/MgFe-LDF and V2O5-F both show a narrower peak than the spectrum of MgFe-V-LDF. Two peaks at V $2p_{3/2}$ binding energies of about 516.6 and 517.7 eV, assigned to V_2O_5 and VOF_x species, respectively. However, the relative content of VOF_x species in V/MgFe-LDF and V_2O_5-F is much lower than that of MgFe-V-LDF. Tab. S5 shows the XPS data obtained by using a peak-fitting program. It is important to note that the MgFe-V-LDF possesses the highest VOF_x concentration (about 40.6%), which is almost 6 times higher than that of V_2O_5-F, and the molar ratio of VOF_x/V_2O_5 as high as 0.68. This further confirms that V species in polyvanadate form (such as crystalline V_2O_5) are stable in fluorinated environments, while highly dispersed monovanadates can be fluorinated to VOF_x species. Hence, we speculated that this highly dispersed VOF_x species is the main active center for gas-phase dehydrofluorination reactions.

To further investigate the difference in the dispersion of V species in MgFe-LDF, after its introduction into VO_3^- by intercalation or supporting, the EDX mapping experiments were performed on MgFe-V-LDF and V/MgFe-LDF. As shown in Fig. 8a, all the elements in the MgFe-V-LDF, including Mg, Fe, V, F and O are uniformly distributed in a sheet-like profile, indicating that V species are highly dispersed in MgFe-V-LDF. In addition, the homogeneous dispersion of V, F and O elements further indicates that the V species (such as VOF_x or V_2O_5) are highly dispersed in MgFe-V-LDF. Fig. 8b shows the EDX mapping of V/MgFe-LDF, the Mg, Fe, O and F are relatively uniformly dispersed, but the content of F elements is significantly lower than that MgFe-V-LDF. It further confirms that the concentration of FeF_3 or other metal fluorides in V/MgFe-LDF is low. It is worthy to highlight that the distribution of V elements in V/MgFe-LDF showed a regional enrichment. It implies that the V_2O_5 is distributed on V/MgFe-LDF with large particles, which is consistent with the XPS and XRD results.

The active center of the gas-phase dehydrofluorination reaction is thought to be the surface Lewis acid site [43]. As a result, pyridine-FTIR experiments on the surface acid structure of representative catalysts were performed. Fig. 9a shows four weaker absorption bands in MgFe-LDF at 1446, 1492, 1579, and 1607 cm^{-1}, indicating the presence of small amounts of Lewis acid sites [44]. After the introduction of V species, the amount of Lewis acid sites in LDF catalysts is significantly elevated. Remarkably, the MgFe-V-LDF possesses the strongest band intensities than that of V/MgFe-LDF at 1450, 1490, 1577 and 1614 cm^{-1}, indicating that the MgFe-V-LDF possesses larger amount of Lewis acid sites. The enhanced acidity of the MgFe-V-LDF surface suggests the formation of a new species with a higher acid content than crystalline V_2O_5. Obviously, pyridine absorption peaks at Brønsted acid sites were also observed in MgFe-V-LDF at 1545 and 1640 cm^{-1} [45].
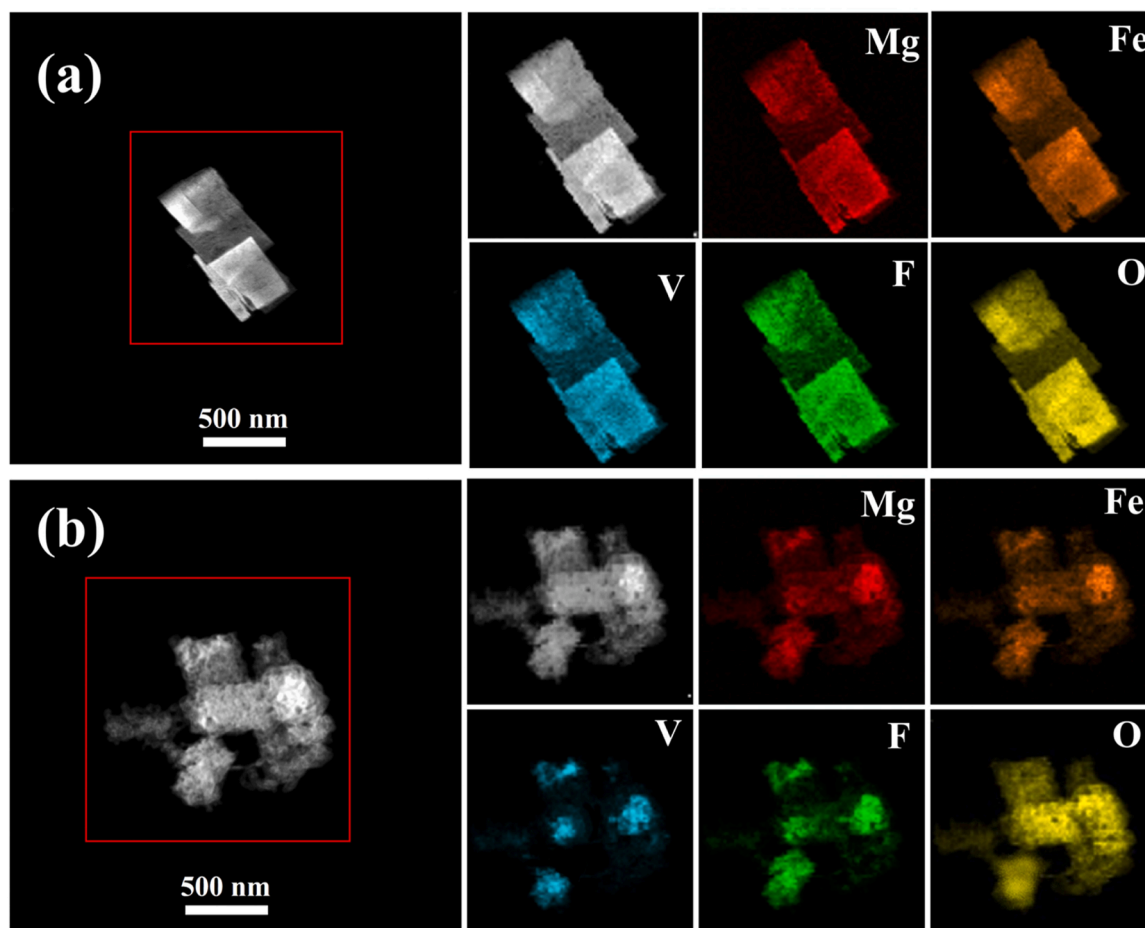

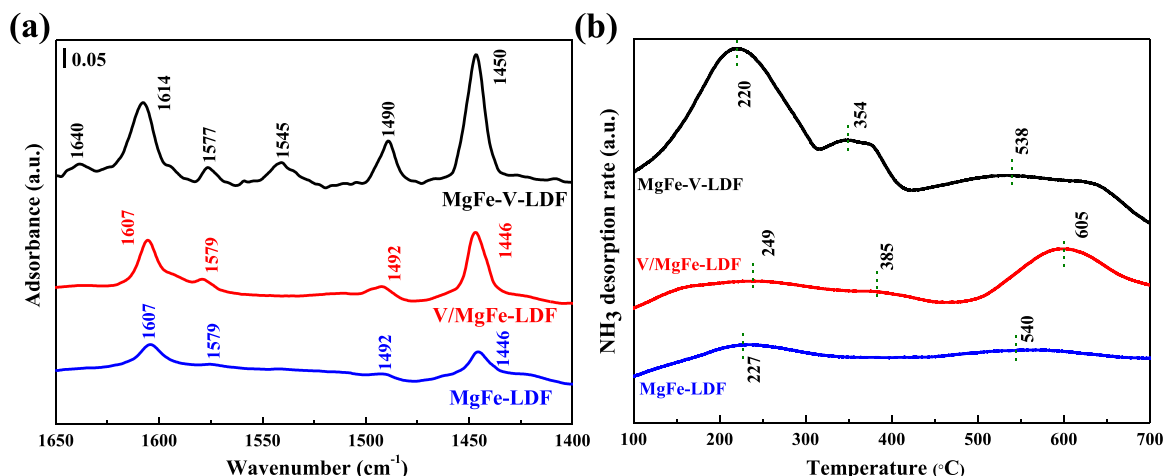**Fig. 8.** EDX Mapping of (a) MgFe-V-LDF and (b) V/MgFe-LDF.

Fig. 9. (a) Pyridine-FTIR and (b) NH$_3$-TPD profiles of MgFe-LDF, V/MgFe-LDF and MgFe-V-LDF.

Above conclusion of pyridine-FTIR is further reinforced by NH$_3$-TPD results. As displayed in Fig. 9b, weak NH$_3$ desorption peaks were detected in MgFe-LDF at both 227 and 540 °C, indicating that there are only a few acidic sites on its surface. Accordingly, its initial activity of dehydrofluorination was low and rapidly deactivated (Fig. 1a). After the introduction of V species, the amount of acid sites in LDF catalysts is dramatically increased. Tow weak NH$_3$ desorption peaks are detected at 249 and 385 °C for V/MgFe-LDF, and a significant NH$_3$ desorption peak is detected at 605 °C, indicating the presence of a huge number of strong acid sites on the surface of V/MgFe-LDF. It is well known that coke and polymer-like deposits form primarily on the strong acid sites of the catalyst in gas-phase dehydrofluorination reactions [46]. The NH$_3$-TPD profiles reveal that the MgFe-V-LDF shows a noteworthy NH$_3$ desorption peak at temperature of 220 °C, and the peak at 538 °C is very weak, which suggests that the catalyst contain large amounts of weak acidic sites. Additionally, MgFe-V-LDF displayed the highest NH$_3$ desorption peak area compared to MgFe-LDF and V/MgFe-LDF, indicating that new species with a higher acid amount than V$_2$O$_5$ and Fe$_2$O$_3$ were formed on its surface. In fact, the data from Raman and XPS (Fig. 6b and Fig. 7) also confirm the presence of more FeF$_3$ and VOF$_x$ species in MgFe-V-LDF. F attracts the electrons of V and Fe in these species, resulting in a greater number of acid sites in these species.

Based on the results of pyridine-FTIR and NH$_3$-TPD, MgFe-V-LDF possessed more Lewis acid sites than that of MgFe-LDF and V/MgFe-LDF, and the metal fluoride acidic sites are formed by coordinatively unsaturated metal sites [47]. Hence, to investigate the amounts of coordinatively unsaturated metal sites of over various LDF catalysts, the EPR spectra were recorded. As shown in Fig. 10, all three catalysts exhibit a clear signal at g = 2.004, which is the typical oxygen vacancy character [48]. Pure MgFe-LDF has very few oxygen vacancies, but after adding V species, the LDF catalyst's oxygen vacancy count increased significantly. In addition, the EPR spectrum of MgFe-V-LDF shows a conspicuous signal peak and the intensity is almost three times higher than V/MgFe-LDF. It is attributed to that the V$_2$O$_5$ highly dispersed in MgFe-V-LDF is converted to VOF$_x$ after pre-fluorination treatment. During this process, the NH$_4$F decomposes to NH$_3$ and HF, where the NH$_3$ undergoes oxidation on V$_2$O$_5$ in the MgFe-V-LDF or V/MgFe-LDF catalyst. Simultaneously, the V^{5+} species in V$_2$O$_5$ are transformed into lower valence vanadium species such as V^{4+} or V^{3+}. The application of V-based catalysts in the NH$_3$-SCR reaction has been extensively reported [49,50], and the highly dispersed vanadium oxides possess higher oxidation activity. Hence, compared to V/MgFe-LDF, more V^{4+} or V^{3+} species are present in MgFe-V-LDF and possess more oxygen vacancies. Similarly, the O 1 s XPS spectra of MgFe-V-LDF and V/MgFe-LDF also confirm this result. As demonstrated on Fig. S12, the MgFe-V-LDF and V/MgFe-LDF are both deconvoluted into three oxygen species. The
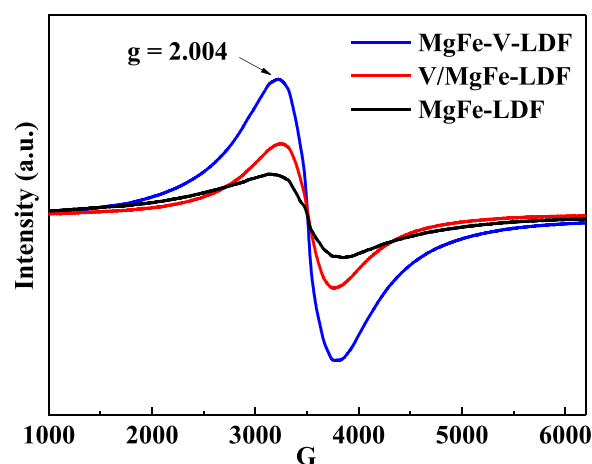

Fig. 10. EPR spectra of MgFe-V-LDF, MgFe-LDF and V/MgFe-LDF measured at room temperature.

component at binding energy of 530.0–529.9 eV is assigned to surface lattice oxygen (named as O$_L$) species in the catalyst, while peak at binding energy of 531.5–531.7 eV is attributed to surface oxygen species (named as O$_V$) adsorbed on the oxygen vacancies. The last peak located at 533.1–533.3 eV is caused by the presence of physically-adsorbed oxygen species (named as O$_W$) from hydroxyls or water species [51]. The relative contents of O species on MgFe-V-LDF and V/MgFe-LDF surface were calculated with XPS data, and the results are listed in Tab. S6. The relative content of O$_L$ species in MgFe-V-LDF is 45.1% much higher than that of V/MgFe-LDF. Accordingly, the MgFe-V-LDF presents more Lewis acidic sites, which is consistent with the pyridine-FTIR and NH$_3$-TPD results. In addition, almost no oxygen vacancies could be detected for pure V$_2$O$_5$-F (Fig. S13), indicating that only a small amounts of Lewis acid sites for V$_2$O$_5$-F.

3.4. Catalytic activity

To investigate the difference in the catalytic activity of dehydrofluorination reaction after its introduction of VO$_3^-$ by intercalation or supporting. The representative catalyst was tested for HFC-245fa dehydrofluorination at 350 °C with a GHSV of 750 h^{-1}. Fig. 11a and Fig. S14 demonstrate the stability of the prepared catalysts. On pure MgFe-LDF, HFC-245fa conversion decreases from 47% to 4% after 20 h, which is connected to the tiny number of Lewis acidic sites on its surface. After the supporting of V species, the catalytic activity is significantly
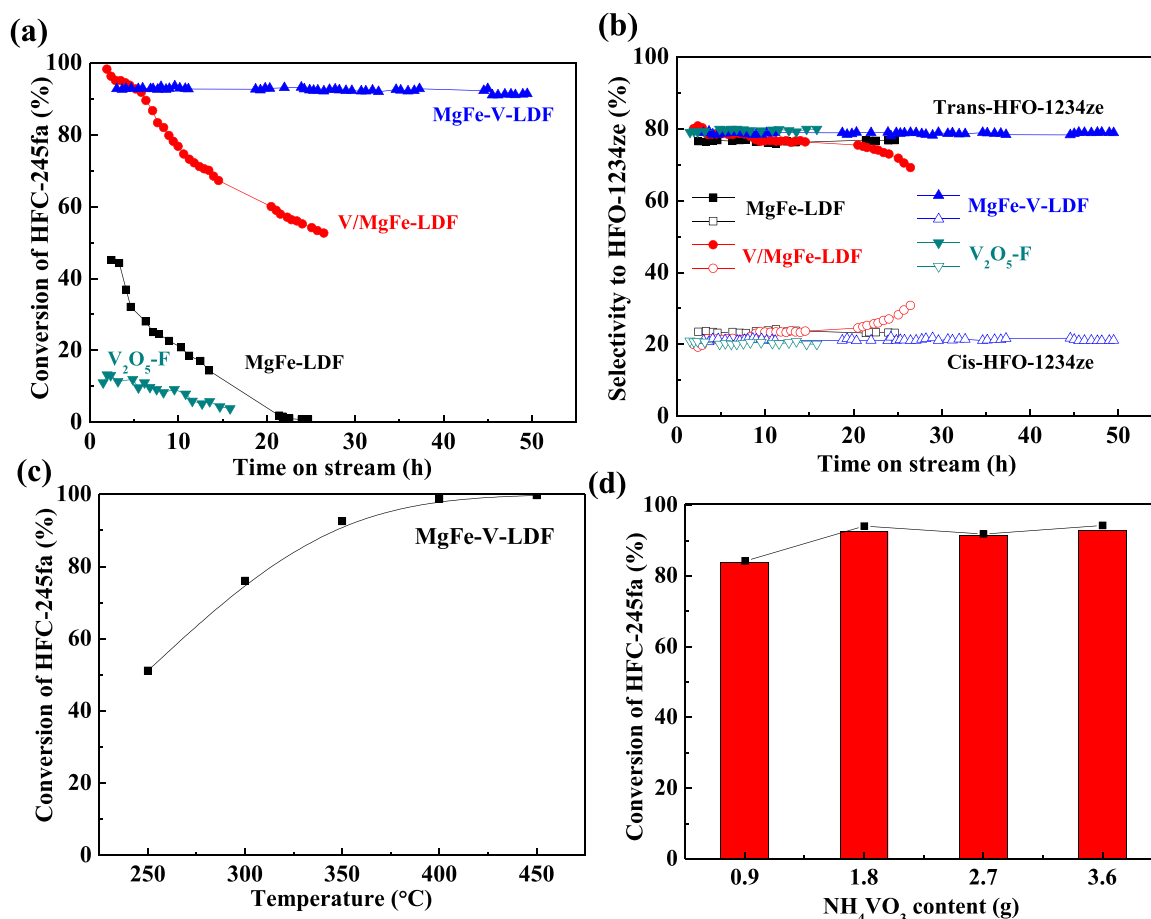
Fig. 11. (a) Conversion of HFC-245fa and (b) Selectivity to trans-HFO-1234ze and cis-HFO-1234ze over representative catalysts (reaction condition: atmospheric pressure, GHSV = 750 h^{-1}, N$_2$/HFC-245fa = 10/4), (c) Conversion of HFC-245fa dehydrofluorination over MgFe-V-LDF as a function of reaction temperature and (d) Conversion of HFC-245fa over MgFe-V-LDF at different content of NH$_4$VO$_3$ introduction.

enhanced. HFC-245fa conversion on V/MgFe-LDF was high (98–93%) for the first 4 h, but gradually deactivated during the subsequent reactions, with conversion dropping to 50% after 25 h. This deactivation was caused by the carbon deposited on a large number of strong acid sites on its surface. By contrast, MgFe-V-LDF possesses the higher activity than that of V/MgFe-LDF and MgFe-LDF. The HFC-245fa conversion reaches a maximum (about 93%), and no significant deactivation is observed after 50 h. The presence of a large amounts of highly dispersed VOF$_x$ in MgFe-V-LDF thus possess more oxygen vacancies and generate a large number of weak Lewis acidic sites. Hence, the MgFe-V-LDF exhibit the highest catalytic activity and stability. Interestingly, pure V$_2$O$_5$-F is barely active for the dehydrofluorination of HFC-245fa at 350 °C, implying that the MgFe-LDF host is an essential component of the catalyst composition. Based on the activity test of representative catalysts, we believed that the highly dispersed V species in the MgFe-V-LDF (such as VOF$_x$) are more active than bulk V$_2$O$_5$ in V$_2$O$_5$-F or V/MgFe-LDF. It has been reported in the literature that isolated VO$_4$ tetrahedral or VO$_x$ species expose more active sites with higher TOF values than crystalline V$_2$O$_5$. For example, Linke et al. [52] reported that isolated VO$_x$ species have higher catalytic activity than crystalline V$_2$O$_5$ in VO$_x$/MCM catalysts for the dehydrogenation of isobutane due to their higher number of V^{3+} and V^{4+} sites. To further investigate the chemical state of V species in MgFe-V-LDF after reaction, XPS and XRD characterization analyses of MgFe-V-LDF-spent were carried out. As shown in Fig. S15, there is no significant difference in the position and intensity of the characteristic diffraction peaks for MgFe-V-LDF-spent and MgFe-V-LDF-fresh, and no new species generation is observed. Similarly, the generation of VF$_3$ species or other new

fluorides are not detected in the V 2p XPS spectra of MgFe-V-LDF-spent. The V species in MgFe-V-LDF-spent are mainly present as V$_2$O$_5$ and VOF$_x$ species (Fig. S16). Furthermore, MgFe-V-LDF has more stable selectivity than V/MgFe-LDF, with trans-HFO-1234ze selectivity of 79% and cis-HFO-1234ze selectivity of 21%, respectively (Fig. 11b). We also investigated the effect of reaction temperature on the catalytic activity of the MgFe-V-LDF catalyst because the dehydrofluorination of HFC-245fa is an endothermic reaction. As displayed in Fig. 11c, the conversion of HFC-245fa onto MgFe-V-LDF increases with reaction temperature, and it is close to 100% when the reaction temperature is 400 °C. To investigate the content of VO$_3^-$, which exhibits the highest activity for HFC-245fa dehydrofluorination over MgFe-V-LDF, the MgFe-V-LDF catalysts with different VO$_3^-$ content (0.9, 2.7 and 3.6 g NH$_4$VO$_3$) were also tested for this reaction. As shown in Fig. 11d, the HFC-245 conversion increases from 82% to 93% as the NH$_4$VO$_3$ content increases from 0.9 to 1.8 g. However, the catalyst activity does not increase significantly as the NH$_4$VO$_3$ content continues to increase (1.8–3.6 g). This is due to the special structure of the layered double hydroxide, the number of interlayer anions is limited. Even if the introduction of NH$_4$VO$_3$ is increased, the excess VO$_3^-$ cannot intercalate into the interlayer of MgFe-LDH and was eventually removed by washing.

4. Conclusion

In summary, we propose a novel strategy for preparing Lewis acid catalysts via host-guest space-confinement. This strategy is widely applicable because it allows the guest interlayer anions and LDHs hosts

to be tailored to specific catalytic requirements in order to design Lewis acid catalysts. In this work, the MgFe-CO_3^{2-}-LDH was selected as host and NH_4VO_3 was selected as guest. During the anion exchange step, interlayer CO_3^{2-} of MgFe-LDH was exchanged by VO_3^- to acquire the MgFe-VO_3^--LDH precursor. Then, MgFe-VO_3^--LDH precursor was partially fluorinated with NH_4F, leading to the formation of MgFe-V-LDF. Due to the confinement effect and strong interaction of highly dispersed interlayer V_2O_5 with host layers, the guest V_2O_5 was anchored in interlamination. Multiple characterization results confirm that after fluorination, V_2O_5 is converted to VOF_x species with a high number of oxygen vacancies. Hence, significant amounts of weak and intermediate Lewis acid sites of MgFe-V-LDF were obtained. It exhibited high activity for the dehydrofluorination of 1,1,1,3,3-pentafluoropropane (HFC-245fa), with HFC-245fa conversion of 93%, which exceeded that of pure V_2O_5-F by roughly 9 times. No significant deactivation was observed after 50 h of reaction, indicating that the catalyst has potential for industrial applications of gas-phase dehydrofluorination.

CRediT authorship contribution statement

Bing Liu: Investigation, Methodology, Validation, Formal analysis, Writing – original draft, Synthesis of catalysts. **Yu Wang**: Formal analysis, Evaluation catalysts. **Yunfan Huang** : Investigation, Formal analysis. **Lijia Liu**: Formal analysis. **Yifan Wei**: Investigation. **Yiwei Sun**: Investigation, Evaluation catalysts. **Xiaoli Wei**: Investigation, Formal analysis. **Wenfeng Han**: Conceptualization, Formal analysis, Validation, Writing – review & editing.

Declaration of Competing Interest

The authors declare that they have no known competing financial interests or personal relationships that could have appeared to influence the work reported in this paper.

Data availability

Data will be made available on request.

Acknowledgements

Appendix A. Supporting information

Supplementary data associated with this article can be found in the online version at doi:10.1016/j.apcatb.2023.122477.

References

[1] S.A. Montzka, G.S. Dutton, P. Yu, E. Ray, R.W. Portmann, J.S. Daniel, L. Kuijpers, B. D. Hall, D. Mondeel, C. Siso, D. Nance, M. Rigby, A.J. Manning, L. Hu, F. Moore, B. R. Miller, J.W. Elkins, An unexpected and persistent increase in global emissions of ozone-depleting CFC-11[J], Nature 557 (2018) 413.

[2] G.J.M. Velders, A.R. Ravishankara, M.K. Miller, M.J. Molina, J. Alcamo, J. S. Daniel, D.W. Fahey, S.A. Montzka, S. Reimann, Preserving Montreal protocol climate benefits by limiting HFCs[J], Science 335 (2012) 922–923.

[3] W. Mao, Y. Bai, B. Wang, W. Wang, H. Ma, Y. Qin, C. Li, J. Lu, Z. Liu, A facile sol-gel synthesis of highly active nano alpha-aluminum fluoride catalyst for dehydrofluorination of hydrofluorocarbons[J], Appl. Catal. B Environ. 206 (2017) 65–73.

[4] T.Y. Song, Z.X. Dong, J.D. Song, X.X. Wang, G.Q. Xie, M.F. Luo, J.Q. Lu, Dehydrochlorination of 1, 1, 2-trichloroethane over SiO_2-supported alkali and transition metal catalysts: tunable selectivity controlled by the acid - base properties of the catalysts[J], Appl. Catal. B Environ. 236 (2018) 368–376.

[5] W. Jia, Y. Chen, M. Liu, X. Liu, X. Liu, J. Yuan, X. Lu, Z. Zhu, Effect of calcination temperature and fluorination treatment on NiF_2-AlF_3 catalysts for dehydrofluorination of 1, 1, 1, 2-tetrafluoroethane to synthesize trifluoroethylene [J], Appl. Catal. A Gen. 571 (2019) 150–157.

[6] G. Coates, H.Y. Tan, C. Kalff, A.J.P. White, M.R. Crimmin, Defluorosilylation of industrially relevant fluoroolefins using nucleophilic silicon reagents[J], Angew. Chem. Int. Ed. 58 (2019) 12514–12518.

[7] W. Mao, Y. Bai, Z. Jia, Z. Yang, Z. Hao, J. Lu, Highly efficient gas-phase dehydrofluorination of 1,1,1,3,3-pentafluoropropane to 1,3,3,3-tetrafluoropropene over mesoporous nano-aluminum fluoride prepared from a polyol mediated sol-gel process[J], Appl. Catal. A Gen. 564 (2018) 147–156.

[8] B. Liu, W. Han, X. Li, L. Li, H. Tang, C. Lu, Y. Li, X. Li, Quasi metal organic framework with highly concentrated Cr_2O_3 molecular clusters as the efficient catalyst for dehydrofluorination of 1,1,1,3,3-pentafluoropropane[J], Appl. Catal. B Environ. (2019) 257.

[9] W. Han, H. Wang, B. Liu, X. Li, H. Tang, Y. Li, H. Liu, PVDF mediated fabrication of freestanding AlF_3 sub-microspheres: facile and controllable synthesis of alpha, beta and theta-AlF_3[J], Mater. Chem. Phys. (2020) 240.

[10] W. Han, C. Zhang, H. Wang, S. Zhou, H. Tang, L. Yang, Z. Wang, Sub-nano MgF_2 embedded in carbon nanofibers and electrospun MgF_2 nanofibers by one-step electrospinning as highly efficient catalysts for 1,1,1-trifluoroethane dehydrofluorination[J], Catal. Sci. Technol. 7 (2017) 6000–6012.

[11] W. Han, B. Liu, X. Li, L. Yang, J. Wang, H. Tang, W. Liu, Combustion synthesis of amorphous Al and Cr composite as the catalyst for dehydrofluorination of 1,1-difluoroethane[J], Ind. Eng. Chem. Res. 57 (2018) 12774–12783.

[12] G. Meissner, K. Kretschmar, T. Braun, E. Kemnitz, Consecutive transformations of tetrafluoropropenes: hydrogermylation and catalytic C-F activation steps at a Lewis acidic aluminum fluoride[J], Angew. Chem. Int. Ed. 56 (2017) 16338–16341.

[13] K. Teinz, S. Wuttke, F. Börno, J. Eicher, E. Kemnitz, Highly selective metal fluoride catalysts for the dehydrohalogenation of 3-chloro-1,1,1,3-tetrafluorobutane[J], J. Catal. 282 (2011) 175–182.

[14] F. Wang, W. Zhang, Y. Liang, Y. Wang, J. Lu, M. Luo, Pd/AlF_3 catalysts for catalytic dehydrofluorination of 1,1,1,3,3-pentafluoropropane[J], Chem. Res. Chin. Univ. 31 (2015) 1003–1006.

[15] Z. Jia, W. Mao, Y. Bai, B. Wang, H. Ma, C. Li, J. Lu, Hollownano-MgF_2 supported catalysts: highly active and stable in gas-phase dehydrofluorination of 1,1,1,3,3-pentafluoropropane[J], Appl. Catal. B Environ. 238 (2018) 599–608.

[16] Y. Guo, P. Gaczynski, K.-D. Becker, E. Kemnitz, Sol-Gel synthesis and characterisation of nanoscopic FeF_3-MgF_2 heterogeneous catalysts with bi-acidic properties[J], Chemcatchem 5 (2013) 2223–2232.

[17] W. Mao, Z. Jia, Y. Bai, Y. Qin, B. Wang, S. Han, W. Zhang, L. Kou, J. Lu, E. Kemnitz, Fe/hollow nano-MgF_2: a green and highly-efficient alternative to classical Cr-based catalysts for the gas-phase fluorination reaction[J], Catal. Sci. Technol. 9 (2019) 3015–3019.

[18] W.T. Broomhead, W. Tian, J.E. Herrera, Y.-H.C. Chin, Kinetic coupling of redox and acid chemistry in methanol partial oxidation on vanadium oxide catalysts[J], Acs Catal. 12 (2022) 11801–11820.

[19] E. Kemnitz, Y. Zhu, B. Adamczyk, Enhanced Lewis acidity by aliovalent cation doping in metal fluorides[J], J. Fluor. Chem. 114 (2002) 163–170.

[20] J.D. Song, T.Y. Song, T.T. Zhang, Y. Wang, M.F. Luo, J.Q. Lu, High performance V_2O_5/MgF_2 catalysts for gas-phase dehydrofluorination of 1,1,1,3,3-pentafluoro-propane: support-induced evolution of new active sites[J], J. Catal. 364 (2018) 271–281.

[21] B. Liu, W. Han, A. Chen, L. Li, H. Tang, C. Lu, G. Zhang, Y. Li, X. Li, Confinement of AlF_3 in MOF derived structures for the formation of 4-fold coordinated Al and significantly improved dehydrofluorination activity[J], Chem. Eng. J. 394 (2020), 124946.

[22] J. Jin, X. Han, Y. Fang, Z. Zhang, Y. Li, T. Zhang, A. Han, J. Liu, Microenvironment engineering of ru single-atom catalysts by regulating the cation vacancies in NiFe-layered double hydroxides[J], Adv. Funct. Mater. (2022) 32.

[23] B. Jiang, Z. Xi, F. Lu, Z. Huang, Y. Yang, J. Sun, Z. Liao, J. Wang, Y. Yang, Ce/MgAl mixed oxides derived from hydrotalcite LDH precursors as highly efficient catalysts for ketonization of carboxylic acid[J], Catal. Sci. Technol. 9 (2019) 6335–6344.

[24] S. Xia, X. Zhang, X. Zhou, Y. Meng, J. Xue, Z. Ni, The influence of different Cu species onto multi-copper-contained hybrid materials' photocatalytic property and mechanism of chlorophenol degradation[J], Appl. Catal. B Environ. 214 (2017) 78–88.

[25] W. Peng, Y. Li, B. Yuan, R. Hu, Z. Luo, M. Zhu, A dealloyed bulk FeNi pattern with exposed highly active facets for cost-effective oxygen evolution[J], Appl. Catal. B Environ. (2022), 122171.

[26] C. Dang, W. Yang, J. Zhou, W. Cai, Porous Ni-Ca-Al-O bi-functional catalyst derived from layered double hydroxide intercalated with citrate anion for sorption-enhanced steam reforming of glycerol[J], Appl. Catal. B Environ. (2021) 298.

[27] Z. Liu, R. Ma, M. Osada, N. Iyi, Y. Ebina, K. Takada, T. Sasaki, Synthesis, anion exchange, and delamination of Co−Al layered double hydroxide: assembly of the exfoliated nanosheet/polyanion composite films and magneto-optical studies[J], J. Am. Chem. Soc. 128 (2006) 4872–4880.

[28] Y. Xu, J. Li, J. Zhou, Y. Liu, Z. Wei, H. Zhang, Layered double hydroxides supported atomically precise Au-n nanoclusters for air oxidation of benzyl alcohol: effects of size and active site structure[J], J. Catal. 389 (2020) 409–420.

[29] H. Feng, J. Yu, L. Tang, J. Wang, H. Dong, T. Ni, J. Tang, W. Tang, X. Zhu, C. Liang, Improved hydrogen evolution activity of layered double hydroxide by optimizing the electronic structure[J], Appl. Catal. B Environ. (2021) 297.

[30] M. Zhang, Z. Luo, M. Zhou, G. Zhang, K.A. Alamry, L.A. Taib, A.M. Asiri, X. Wang, Ni-Co layered double hydroxides cocatalyst for sustainable oxygen photosynthesis [J], Appl. Catal. B Environ. 210 (2017) 454–461.

[31] A.L. Villa, D.E. De Vos, F. Verpoort, B.E. Sels, P.A. Jacobs, A study of V-pillared layered double hydroxides as catalysts for the epoxidation of terpenic unsaturated alcohols[J], J. Catal. 198 (2001) 223–231.

[32] P. Zhang, X. Zeng, X. Wen, C. Yang, S. Ouyang, P. Li, Z. Gu, D. Wu, R.L. Frost, Insights into efficient removal and mechanism for ammonium from aqueous solution on tricalcium aluminate[J], Chem. Eng. J. 366 (2019) 11–20.

[33] G. Fischer, X.L. Cao, N. Cox, M. Francis, The FT-IR spectra of glycine and glycylglycine zwitterions isolated in alkali halide matrices[J], Chem. Phys. 313 (2005) 39–49.

[34] W. Chen, B. Wu, Y. Wang, W. Zhou, Y. Li, T. Liu, C. Xie, L. Xu, S. Du, M. Song, D. Wang, Y. Liu, Y. Li, J. Liu, Y. Zou, R. Chen, C. Chen, J. Zheng, Y. Li, J. Chen, S. Wang, Deciphering the alternating synergy between interlayer Pt single-atom and NiFe layered double hydroxide for overall water splitting[J], Energy Environ. Sci. 14 (2021) 6428–6440.

[35] A. Khodakov, B. Olthof, A.T. Bell, E. Iglesia, Structure and catalytic properties of supported vanadium oxides: support effects on oxidative dehydrogenation reactions[J], J. Catal. 181 (1999) 205–216.

[36] Y. Ganjkhanlou, T.V.W. Janssens, P.N.R. Vennestrom, L. Mino, M.C. Paganini, M. Signorile, S. Bordiga, G. Berlier, Location and activity of VO_x species on TiO_2 particles for NH_3-SCR catalysis[J], Appl. Catal. B Environ. (2020) 278.

[37] S.M. Coman, M. Verziu, A. Tirsoaga, B. Jurca, C. Teodorescu, V. Kuncser, V. I. Parvulescu, G. Scholz, E. Kemnitz, NbF_5-AIF_3 catalysts: design, synthesis, and application in lactic acid synthesis from cellulose[J], Acs Catal. 5 (2015) 3013–3026.

[38] A. Held, J. Kowalska-Kus, K. Nowinska, K. Gora-Marek, Potassium-modified silica-supported vanadium oxide catalysts applied for propene epoxidation[J], J. Catal. 347 (2017) 21–35.

[39] X. Fan, Y. Liu, S. Chen, J. Shi, J. Wang, A. Fan, W. Zan, S. Li, W.A. Goddard III, X.-M. Zhang, Defect-enriched iron fluoride-oxide nanoporous thin films bifunctional catalyst for water splitting[J], Nat. Commun. (2018) 9.

[40] Y. Guo, A. Lippitz, P. Saftien, W.E.S. Unger, E. Kemnitz, Tuning the surface properties of novel ternary iron(iii) fluoride-based catalysts using the template effect of the matrix[J], Dalton Trans. 44 (2015) 5076–5085.

[41] M. Jones, G.J. Hutching, D.J. Willock, J. Scott, S.H. Taylor, Zinc promoted alumina catalysts for the fluorination of chlorofluorocarbons[J], J. Catal. 364 (2018) 102–111.

[42] X. Liu, J. Wu, S. Zhang, Q. Li, Z. Wu, J. Zhang, Evaluation of an ε-manganese (IV) oxide/manganese vanadium oxide composite catalyst enriched with oxygen vacancies for enhanced formaldehyde removal[J], Appl. Catal. B Environ. 320 (2023), 121994.

[43] W. Han, H. Yang, L. Wang, B. Liu, X. Wei, A. Chen, W. Song, H. Tang, Y. Li, Confined aluminum fluoride layers derived from the in situ etching of Ti_3AlC_2 as the robust catalyst for dehydrofluorination reaction[J], Appl. Surf. Sci. (2021) 538.

[44] P. Carniti, A. Gervasini, F. Bossola, Dal, V. Santo, Cooperative action of Bronsted and Lewis acid sites of niobium phosphate catalysts for cellobiose conversion in water[J], Appl. Catal. B Environ. 193 (2016) 93–102.

[45] Y. Qi, X. Xiao, Y. Mei, L. Xiong, L. Chen, X. Lin, Z. Lin, S. Sun, B. Han, D. Yang, Y. Qin, X. Qiu, Modulation of Bronsted and Lewis acid centers for $NixCo_3$-xO_4 spinel catalysts: towards efficient catalytic conversion of lignin[J], Adv. Funct. Mater. (2022) 32.

[46] W. Han, B. Liu, Y. Kang, Z. Wang, W. Yu, H. Yang, Y. Liu, J. Lu, H. Tang, Y. Li, W. Song, Experimental and DFT mechanistic study of dehydrohalogenation of 1-chloro-1,1-difluoroethane over metal fluorides[J], Ind. Eng. Chem. Res. 58 (2019) 18149–18159.

[47] T. Krahl, E. Kemnitz, Aluminium fluoride – the strongest solid Lewis acid: structure and reactivity[J], Catal. Sci. Technol. 7 (2017) 773–796.

[48] G. Ou, Y. Xu, B. Wen, R. Lin, B. Ge, Y. Tang, Y. Liang, C. Yang, K. Huang, D. Zu, R. Yu, W. Chen, J. Li, H. Wu, L.-M. Liu, Y. Li, Tuning defects in oxides at room temperature by lithium reduction[J], Nat. Commun. (2018) 9.

[49] L. Jiang, Q. Liu, G. Ran, M. Kong, S. Ren, J. Yang, J. Li, V_2O_5-modified Mn-Ce/AC catalyst with high SO_2 tolerance for low-temperature NH_3-SCR of NO[J], Chem. Eng. J. 370 (2019) 810–821.

[50] X. Liu, J. Li, X. Li, Y. Peng, H. Wang, X. Jiang, L. Wang, NH3 selective catalytic reduction of NO: A large surface TiO_2 support and its promotion of V_2O_5 dispersion on the prepared catalyst[J], Chin. J. Catal. 37 (2016) 878–887.

[51] X. Hu, Y. Wang, R. Wu, L. Zhao, X. Wei, Y. Zhao, Effects of zirconia crystal phases on the catalytic decomposition of N_2O over Co_3O_4/ZrO_2 catalysts[J], Appl. Surf. Sci. (2020) 514.

[52] U. Rodemerck, M. Stoyanova, E.V. Kondratenko, D. Linke, Influence of the kind of VO_x structures in VO_x/MCM-41 on activity, selectivity and stability in dehydrogenation of propane and isobutane[J], J. Catal. 352 (2017) 256–263.